Applied Physics Letters

Error-free data transmission through fast broadband all-optical modulation in graphene–silicon optoelectronics

Cite as: Appl. Phys. Lett. **116**, 221106 (2020); https://doi.org/10.1063/5.0006596
Submitted: 04 March 2020 . Accepted: 24 May 2020 . Published Online: 05 June 2020

Hao Zhou, Xiaoliang Zhu, Tingyi Gu, Jiagui Wu, Guoliang Deng, Shu-Wei Huang, Noam Ophir, Mingbin Yu, Dim-Lee Kwong, Shouhuan Zhou, Keren Bergman, and Chee Wei Wong

Applied Physics Letters ARTICLE scitation.org/journal/apl

Error-free data transmission through fast broadband all-optical modulation in graphene–silicon optoelectronics

Cite as: Appl. Phys. Lett. **116**, 221106 (2020); doi: 10.1063/5.0006596
Submitted: 4 March 2020 · Accepted: 24 May 2020 ·
Published Online: 5 June 2020

Hao Zhou,[1,2,a)] Xiaoliang Zhu,[3] Tingyi Gu,[2,3,4] Jiagui Wu,[2] Guoliang Deng,[1] Shu-Wei Huang,[5] Noam Ophir,[3] Mingbin Yu,[6] Dim-Lee Kwong,[6] Shouhuan Zhou,[1] Keren Bergman,[3] and Chee Wei Wong[2,7,a)]

AFFILIATIONS

[1]College of Electronics and Information Engineering, Sichuan University, Chengdu 610064, China
[2]Optical Nanostructures Laboratory, Columbia University, New York, New York 10027, USA
[3]Department of Electrical Engineering, Columbia University, New York, New York 10027, USA
[4]Department of Electrical and Computer Engineering, University of Delaware, Newark, Delaware 19716, USA
[5]Department of Electrical, Computer, and Energy Engineering, University of Colorado Boulder, Boulder, Colorado 80309, USA
[6]The Institute of Microelectronics, Singapore 117685, Singapore
[7]Fang Lu Mesoscopic Optics and Quantum Electronics Laboratory, University of California, Los Angeles, California 90095, USA

[a)]**Authors to whom correspondence should be addressed:** zhoufirst@scu.edu.cn and cheewei.wong@ucla.edu

ABSTRACT

Ultrafast third order nonlinearity in silicon photonics is promising for all-optical signal processing beyond 100 Gbit/s. However, the coexistence of slower dynamical responses, such as mesoscopic Drude free-carrier plasma or thermal nonlinearities, degrades high-speed signal integrity. Here, we introduce atomic-layer graphene onto the silicon nanophotonic platform to leverage its unique nondegenerate two-photon absorption and ultrafast carrier dynamics, demonstrating broadband and fast bitrate transmission through cross-absorption modulation. Multichannel error-free optical transmission across telecommunication C- and L-bands is demonstrated with 10^{-12} bit-error rates at a data transmission rate of 1 Gbps. The bandwidth of the hybrid silicon–graphene structure is demonstrated at least up to 25 GHz. The broadband cross-absorption modulation over 640 nm in graphene–silicon optoelectronics provides a promising scalable material platform for high-speed all-optical signal processing.

Graphene has tremendous potential across nanoscale electronics and photonics.[1,2] Different from conventional materials, graphene offers wide frequency band operation because of its bandgap absence and linear dispersion at optical frequencies, which ranges from visible to near-infrared including optical communication frequencies.[3–6] In addition to a wideband 2.3% constant absorption defined by the fine-structure constant, graphene has a large optical nonlinearity, including a large two-photon absorption (TPA) coefficient.[4,7] Furthermore, the atomic layer thickness, remarkably high carrier mobility, and ultrafast relaxation dynamics of hot Dirac fermions support high-speed graphene devices.[8–11] These ultrafast characteristics of graphene make it a promising candidate for chip-scale all-optical communications and signal processing.

Here, we examine the TPA-induced broadband cross-absorption modulation (XAM) in graphene–silicon devices for all-optical switching. Ultrafast TPA has been proposed for all-optical XAM in silicon waveguides.[12,13] The lingering free-carrier absorption limits the response. A rather long nanoscale waveguide path or applying reverse bias is needed to ensure the free carriers' recombination.[14,15]

Currently, graphene-based modulators are based on the intrinsic response of graphene itself, such as tunable linear absorption at its Fermi level, with a maximum modulation bandwidth up to 35 GHz and a data rate up to 50 Gb/s.[3,16–20] Supporting photonic structures have also been designed for improved photonic coupling to the graphene layer.[21–24] Other all-optical modulation mechanisms were demonstrated through graphene-assisted free carrier absorption, thermo-optic effect, saturable absorption, Kerr nonlinearity, and plasmonics.[25–31] Their pulse width ranged from microseconds to 260 fs while only demonstrating a modulation speed of ∼kHz. In this paper, the free carrier lifetime of the device is greatly reduced to less than 40 ps (resolution limited by the instruments) by transferring graphene onto the photonic crystal waveguide (PhCWG). Instead of sophisticated design or electrical integration, the nonlinear switching coefficient and response speed are enhanced in a 20-μm long device. The

maximum 85% modulation depth, 640 nm working band, and 1 Gbps error-free data transmission with at least 25 GHz potential all-optical modulation are achieved simultaneously.

Figure 1(a) illustrates the physical processes in our graphene–silicon XAM broadband transmission architecture. When the graphene layer is directly brought into contact with the silicon waveguide, a Schottky junction is formed because of the different work function between graphene and silicon. Nondegenerate TPA (ND-TPA) arises with one photon from the pump and one from the probe, which has a collective sum of energies higher than that of the material bandgap. The photons of probe light will be absorbed alone with the photons of the pump light during the ND-TPA process, resulting in a dark pulse XAM [Fig. 1(b), process 1]. Meanwhile, electron and hole distributions are excited to nonequilibrium by the TPA interband transition processes and then rapidly thermalize and cool to equilibrium by intraband scattering. The resulting generation of carriers can be broadband, as well as the following ultrafast carrier relaxation, and these processes last less than the sub-pico-second timescale in both silicon and graphene, allowing the broadband and fast pump-to-signal data transfer.[9,10,32,33] Photo-generated carriers recombine (FCR) in graphene on the picosecond scale, while carriers generated in monolithic silicon recombine slowly and form a long free-carrier absorption (FCA) tail [Fig. 1(b), process 2]. In the graphene–PhCWG structure, the carriers generated in silicon can vertically transfer to graphene with a high transfer rate through the built-in field at the graphene–silicon interface. Then, the carriers recombine with high surface recombination velocities, equivalently decreasing the lifetime of free carriers. This ultrafast process was demonstrated in our graphene–silicon Schottky photodetectors,[34,35] and was usually suppressed by surface passivation to increase the carriers' lifetime to enhance the photoresponse in applications of graphene–Si Schottky solar cells.[36]

Our graphene–silicon PhCWG device is a W1 line defect waveguide configuration with a length of 20 μm. CVD-grown monolayer graphene covers the PhCWG well through wet transfer,[37,38] as examined by Raman spectroscopy and scanning electron microscopy [SEM, Fig. 1(c)]. Raman spectra collected at the center of the graphene–PhCWG and intensity mapping of the 2D peak indicate that the device is well covered by a slightly p-doped graphene layer.[39,40] The total insertion loss of the device is ~16 dB, including 5 dB graphene absorption loss. The linear loss introduced by graphene depends on the material quality and Fermi level of graphene, which can be further controlled by doping to eliminate the linear loss, while the ND-TPA modulation process can still exist. Chip transmission is measured using tunable lasers [Fig. 1(d)], scanning from 1490 nm to 1675 nm and 1935 nm, as well as 1950 nm. A flat transmission of about −16 dB is observed with a fluctuation less than 3 dB. Our short PhCWG length (20 μm) allows a smaller photonic crystal mode onset extinction ratio in the solely silicon PhCWG transmission, enabling the large optical bandwidth demonstration.

The testing setup for XAM is shown in Fig. 1(e). The pump is provided by a mode-locked fiber laser with ~3 ps pulses centered at 1550 nm. After passing through a fiber polarization controller (PC), the pulses are modulated by a $LiNbO_3$ modulator and a programmable pattern generator (PPG) outputting the pseudo-random binary sequence (PRBS, length 2^7–1 bits). The pump pulses are subsequently amplified by an erbium-doped fiber amplifier (EDFA 1). To generate the dual-pulse to watch the dynamical response limit of our graphene–PhCWG system, a tunable optical delay was built using fiber. The pulse pump light and continuous wave (CW) probe light are combined by a wavelength division multiplexer (WDM) and are coupled into our chip with a lensed fiber coupler. The output transmission is collected by another lensed fiber and sent to a tunable bandpass filter, which filters out the pump light. The probe signal is then amplified by an EDFA 2 and is examined using a bit-error-rate tester (BERT) and a 20 GHz digital communication analyzer (DCA). When we switch between PhCWG chips with and without graphene, calibrations are done with a reference waveguide to make sure that the instruments and coupling condition remain the same.

As shown in Fig. 1(f), the weak probe signal shows an early dark pulse because of the cross-absorption driven by ND-TPA. For both the graphene–PhCWG (orange curve) and the monolithic PhCWG (green curve), we observe a similar early dark pulse with a modulation depth of about 65%. However, the relatively slow free-carrier recombination of over 450 ps (Refs. 4 and 14) limits the modulation rate in monolithic silicon. With graphene–silicon implementation, the free carrier goes back to its initial state, right after the ND-TPA (orange curve). The pulse width shown in Fig. 1(f) is about 40 ps, limited by the detector bandwidth. The small peak right behind the main peak is caused by detector ringing.

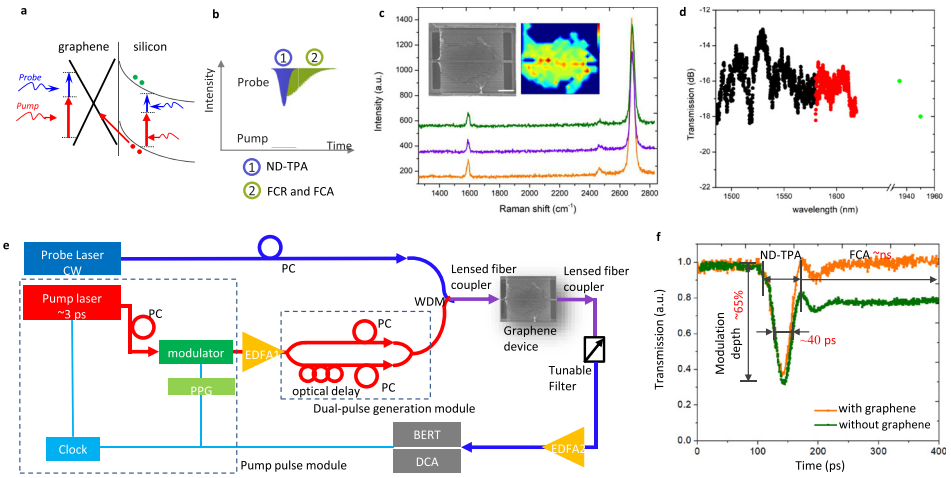

FIG. 1. Ultrafast data transfer through nondegenerate two-photon absorption-based cross-absorption modulation in graphene–silicon optoelectronics. (a) Schematic diagram of ND-TPA-based XAM between the pump and probe lasers in the graphene–PhCWG Schottky junction. (b) Schematic diagram of ND-TPA and the following free carrier recombination (FCR) and free carrier absorption (FCA) process. (c) SEM image and Raman spectra of the graphene-covered PhCWG. Scale bar: 5 μm. (d) Transmission spectrum of the device. Different colors indicate different lasers. (e) Experimental setup including pump-probe and dual-pulse pump generation. (f) Real-time measurement of XAM in the monolithic silicon PhCWG (green curve) and in the graphene–PhCWG (orange curve).

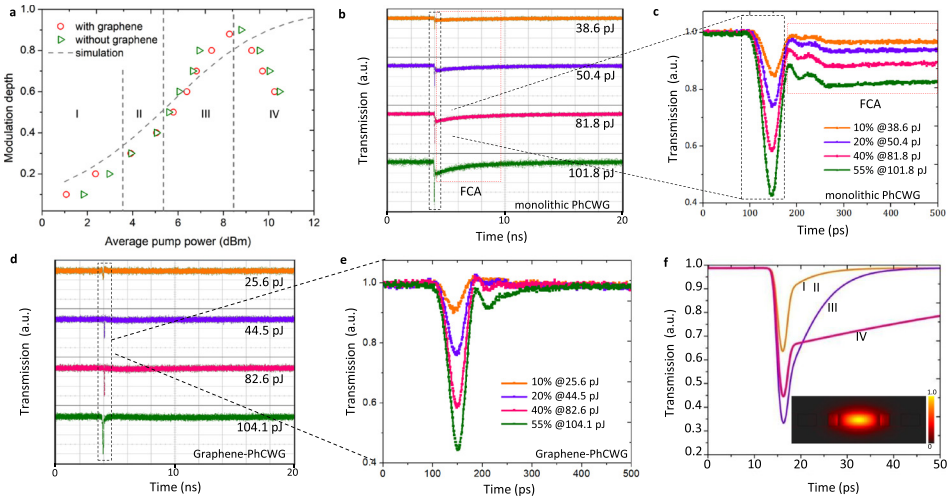

FIG. 2. Graphene cross-absorption modulation at different pump powers. (a) Experimental and simulated (dashed line) results of the graphene–PhCWG (red circles) and the PhCWG (green triangle) modulation depth as a function of pump power at 1543 nm. (b) XAM with different modulation depths in the graphene–PhCWG. (c) Zoom-in of (b). (d) XAM with different modulation depths in the monolithic silicon PhCWG. (e) Zoom-in of (d). (f) Modeled time domain evolution. The inset shows the simulated mode field distribution of TE mode in the graphene–PhCWG structure.

As shown in Fig. 2, the probe wavelength is fixed at 1543 nm with a power of 6 dBm. The pump wavelength is 1550 nm, with a 39 MHz repetition rate, and the average pulse energy gradually increased from 25.6 pJ to 104.1 pJ (average power density 1.55–6.33 GW/cm^2) to achieve a modulation depth from 10% to 55%. The dependence of the modulation depth and pump power in the PhCWG with/without graphene is shown in Fig. 2(a) [corresponding time domain evolution is shown in Figs. 2(b)–2(e)]. Thanks to the ultrahigh TPA coefficient of graphene, the graphene–PhCWG performs better than the PhCWG when the average pump power is below ~3 dBm (modulation depth from 0 to ~30%). ND-TPA dominates the modulation process, and FCA is negligible in the graphene–PhCWG (region I). When the pump power goes on, more free carriers excited by TPA take part in the modulation process, absorb the probe light, and enhance the modulation depth. In region II (modulation depth from ~30% to ~50%), the modulation efficiency is almost the same in the device with/without graphene as free carriers are suppressed by graphene in the graphene–PhCWG hybrid structure. In region III, the modulation depth continues to increase (from ~50% to ~85%), but the recombination tail appears because of high free-carrier densities. In this region, the modulation depth is a bit higher in silicon. This is because of the fact that much more free carriers are generated in silicon than graphene–silicon, and FCA helps to achieve a higher modulation depth in silicon. In region IV, a large number of free-carriers are generated. The presence of FCA, thermal effect, and higher order nonlinear absorption decreases the modulation depth from 85% to 60%. The simulation curve (dashed line) does not decrease when pump power is very high because we only consider the TPA and FCA process in the modeling. Also note that saturable absorption should appear in graphene when the pump power density in the graphene layer reaches a high level (~GW/cm^2). The saturable absorption will increase the transmission of probe light. However, we always see dark pulses of the probe light during the modulation. Hence, the primary fast modulation mechanism in our device is still ND-TPA induced XAM.

Curves in Fig. 2(b) show the XAM in the monolithic PhCWG. The density of free-carriers instantaneously rises with the pump power in the PhCWG, with clear free-carrier relaxation tails even when the modulation is as low as 10% [denoted in the red dashed boxes of Figs. 2(b) and 2(c)]. When the modulation depth reaches ≈55%, the free-carrier recombination time is measured to be nearly 2 ns, which distorts the modulation. The XAM in the graphene–PhCWG is significantly better, as shown in Figs. 2(d) and 2(e). Even when the modulation depth increases to ≈40%, the free-carrier recombination tail is still not observable. When we increase the modulation depth to 55%, the free-carrier recombination tail begins to appear, due to carrier saturation.

To understand the FCA contributions, we model the XAM with the below dynamical nonlinear governing equations:[12,13]

$$\frac{dP_{pump}}{dz}(z,t) = -\alpha P_{pump}(z,t) - \sigma_{FCA} N(z,t) P_{pump}(z,t) - \beta_{\deg} P_{pump}(z,t) P_{pump}(z,t), \quad (1)$$

$$\frac{dP_{probe}}{dz}(z,t) = -\alpha P_{probe}(z,t) - \sigma_{FCA} N(z,t) P_{probe}(z,t) - \beta_{non-\deg} P_{pump}(z,t) P_{probe}(z,t), \quad (2)$$

$$\frac{dN(z,t)}{dt} = \frac{\beta_{\deg}}{2h\nu} P_{pump}(z,t) P_{pump}(z,t) - \frac{N(z,t)}{\tau}, \quad (3)$$

where P_{pump} and P_{probe} are the pump and probe powers, respectively. α is the linear loss, which is about 5 dB/cm in silicon and ≈0.25 dB/μm

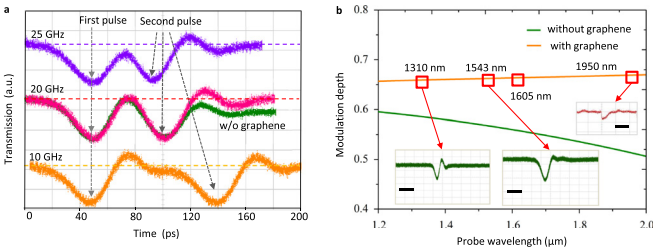

FIG. 3. Probing the modulation dynamics with a dual-pump and broadband graphene–silicon cross-absorption modulation. (a) Dual-pump pulse measurements of the graphene–silicon waveguide. (b) Measured (red open squares) and simulated (orange and green curves) modulation depth at the communication C- and L-bands. The inset shows the example time-domain evolutions at 1310-nm, 1543-nm (scale bar: 50 ps), and 1950 nm (scale bar: 2 ns) probe wavelengths.

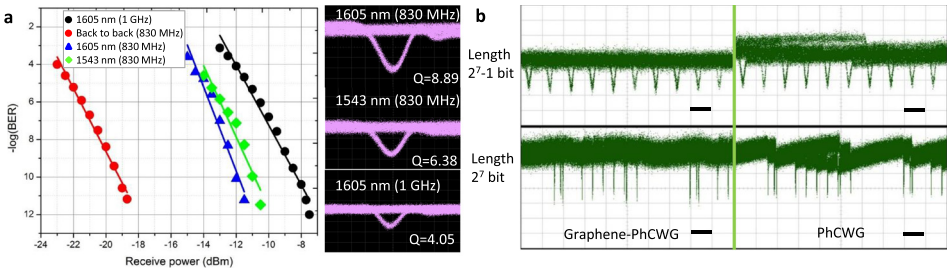

FIG. 4. Bit error rate and quality factor measurements in graphene transmission as well as the pseudo-random binary sequence modulations. (a) BER and measured eye diagrams for 1605 nm and 1543 nm probe wavelengths at different modulation speeds. (b) PRBS-modulated transmission in the graphene–PhCWG and the PhCWG, comparing 2^7–1 bits (scale bar: 200 ps) and 2^7 bits (scale bar: 1 ns).

in the graphene-PhCWG. β_{deg} and $\beta_{non\text{-deg}}$ are the degenerate TPA and nondegenerate TPA coefficients, respectively. σ_{FCA} is the free-carrier cross section, N the carrier density, τ the free-carrier recombination lifetime, z the propagation direction, and ν the optical frequency. The calculated modulation depths for different pump powers are shown in the dashed line plot of Fig. 2(e). The corresponding temporal responses for the four regions of low (I, II), medium (III), and high (IV) pump powers are illustrated in Fig. 2(f).

The free-carrier recombination time is about 1–15 ps in different doped graphene,[9,10] increasing the overall potential modulation rate capacity of the graphene–silicon hybrid. We built a dual-pulse generation module [Fig. 1(c)] with varying inter-pulse delays to examine the graphene–silicon device dynamics. The pump pulse is split by a 50:50 fiber coupler. One of the paths has a tunable optical delay, and then the two pulses are coupled together, forming an interleaved dual-pulse pump with the closest-pulse to closest-pulse repetition rate from 10 GHz to 25 GHz. We send the interleaved dual-pulse pump with the XAM at the tuned pulse-to-pulse separations of 100 ps (10 GHz; orange line), 50 ps (20 GHz; red line), and 40 ps (25 GHz; purple curve) shown in Fig. 3(a). The time trace of each pulse is very clear and does not affect the next pulse, as there is no residual free-carrier tail in the graphene–silicon PhCWG. (At 25 GHz, the dual-pulse has a slight overlap due to the detector bandwidth limit.) We note that the modulation depth is stable and not affected by various modulation speeds. For comparison, we also show the response of the monolithic silicon PhCWG with the green curve in Fig. 3(a) at 20 GHz, and the free-carrier tail is very clear after the second pulse.

We examine the broadband performance of the graphene–PhCWG device as illustrated in Fig. 3(b) (red squares). The pump is kept at 1550 nm, and the probe signal is examined using continuous wave lasers at 1310 nm, 1543 nm, 1605 nm, and 1950 nm. Our broadband modulation measurements span over 640 nm in the graphene–silicon hybrid device. For each probe wavelength, different sets of amplifiers, filters, and photodiodes are used to support this demonstration. The instrumentation performance away from the C- and L-bands is not as good, illustrating a larger overshoot with the 1310 nm detector and a response speed of about 1 ns at 1950 nm. The inset shows the example temporal waveforms at 1543 nm, 1310 nm, and 1950 nm. While 1950 nm and 1310 nm do have smaller transmission intensities than at the C- and L-bands, this is also compensated by optical amplifiers. Our measurements are supported with numerical simulations, shown by the orange solid line of Fig. 3(b), where the modeled modulation depth is almost flat from 1200 nm to 2000 nm, which is better than that in the silicon device (green line) because of the much higher TPA coefficient and the much wider work band in graphene.

To further the investigation of the optical communication system capability, bit-error-rate (BER) and eye-diagram measurements are carried out at communication C- and L-bands. BER curves for the 1543 nm probe (green diamond) and 1605 nm probe (blue triangle) under 830 MHz and 1 GHz modulation are shown in Fig. 4(a). The modulation pattern is return-to-zero (RZ) and the BER reaches a 10^{-11} level, demonstrating error-free transmission. The BER curve for the 1605 nm probe and 1 GHz modulation speed is also examined (black dots), achieving the 10^{-12} BER level. The red dot data show the back-to-back reference measurement, which indicates that the power penalty of our system is about 7 dB. The clear error-free open eye diagrams are presented on the right, and the quality factor (Q factor) is estimated from 4.05 to 8.89.

Next, in Fig. 4(b), we illustrate the XAM output patterns with 1 GHz PRBS pattern input (length 2^7–1 bits). The results are noisier than 1 and 0 RZ data input because the PRBS varying duty cycle would cause transient amplification effects in the EDFA. The best BER here we achieve is $\approx 10^{-4}$. From the DCA output, we observe that although the absorption of the graphene layer increases the noise, the free-carrier combination tail affects the pulses much more, making the XAM pattern and modulation quality in the monolithic silicon device worse than that in graphene implementation.

In this study, we demonstrate a hybrid graphene–silicon PhCWG for high-quality XAM toward optical communication on-chip. We leverage the strong graphene absorption into cross-absorption-based data encoding, achieving more than 55% modulation depth, Q factors up to 8.89, and error-free data transmission up to 1 Gbps with a BER of 10^{-12}. Our approach benefits from the intrinsic ultrafast carrier recombination in atomic layer graphene for fast modulation spanning 640 nm. The broadband zero-bandgap graphene can also interface with III–V materials to further extend the modulation wavelengths. Our broadband, time-domain, and bit-error-rate experiments are supported by our theory and numerical simulations, demonstrating a promising route for chip-scale next-generation all-optical data processing.

AUTHORS' CONTRIBUTIONS

H.Z. and X.Z. contributed equally to this work.

The authors acknowledge valuable discussions and assistance from Zhenda Xie, Christine Chen, Xiaobo Feng, JinLuo Cheng, and Nathalie Vermeulen. This work was supported by the National Science Foundation [Nos. DGE-1069240 (IGERT), DMR-1611598, CBET-1438147, ONR, and FA9550-18-1-0300], the National Natural Science Foundation of China (Grant Nos. 61705148 and 61705149), and the Chinese Scholarship Council.

DATA AVAILABILITY

The data that support the findings of this study are available from the corresponding author upon reasonable request.

REFERENCES

[1]K. S. Novoselov, A. K. Geim, S. V. Morozov, D. Jiang, Y. Zhang, S. V. Dubonos, I. V. Grigorieva, and A. A. Firsov, "Electric field effect in atomically thin carbon films," Science **306**, 666–669 (2004).

[2]F. Bonaccorso, Z. Sun, T. Hasan, and A. C. Ferrari, "Graphene photonics and optoelectronics," Nat. Photonics **4**, 611–622 (2010).

[3]M. Liu, X. Yin, E. Ulin-Avila, B. Geng, T. Zentgraf, L. Ju, F. Wang, and X. Zhang, "A graphene-based broadband optical modulator," Nature **474**, 64–67 (2011).

[4]T. Gu, N. Petrone, J. F. McMillan, A. van der Zande, M. Yu, G. Q. Lo, D. L. Kwong, J. Hone, and C. W. Wong, "Regenerative oscillation and four-wave mixing in graphene optoelectronics," Nat. Photonics **6**, 554–559 (2012).

[5]B. Yao, S. W. Huang, Y. Liu, A. K. Vinod, C. Choi, M. Hoff, Y. Li, M. Yu, Z. Feng, D. Kwong, Y. Huang, Y. Rao, X. Duan, and C. W. Wong, "Gate-tunable frequency combs in graphene–nitride microresonators," Nature **558**, 410–414 (2018).

[6]K. F. Mak, M. Y. Sfeir, Y. Wu, C. H. Lui, J. A. Misewich, and T. F. Heinz, "Measurement of the optical conductivity of graphene," Phys. Rev. Lett. **101**, 196405 (2008).

[7]H. Yang, X. Feng, Q. Wang, H. Huang, W. Chen, A. T. S. Wee, and W. Ji, "Giant two-photon absorption in bilayer graphene," Nano Lett. **11**, 2622–2627 (2011).

[8]F. Xia, T. Mueller, Y. Lin, A. Valdes-Garcia, and P. Avouris, "Ultrafast graphene photodetector," Nat. Nanotechnol. **4**, 839–843 (2009).

[9]P. A. George, J. Strait, J. Dawlaty, S. Shivaraman, M. Chandrashekhar, F. Rana, and M. G. Spencer, "Ultrafast optical-pump terahertz-probe spectroscopy of the carrier relaxation and recombination dynamics in epitaxial graphene," Nano Lett. **8**, 4248–4251 (2008).

[10]D. Sun, Z. Wu, C. Divin, X. Li, C. Berger, W. A. de Heer, P. N. First, and T. B. Norris, "Ultrafast relaxation of excited Dirac fermions in epitaxial graphene using optical differential transmission spectroscopy," Phys. Rev. Lett. **101**, 157402 (2008).

[11]E. J. Lee, S. Y. Choi, H. Jeong, N. H. Park, W. Yim, M. H. Kim, J. Park, S. Son, S. Bae, S. J. Kim, K. Lee, Y. H. Ahn, K. J. Ahn, B. H. Hong, J. Park, F. Rotermund, and D. Yeom, "Active control of all-fibre graphene devices with electrical gating," Nat. Commun. **6**, 6851 (2015).

[12]T. K. Liang, L. R. Nunes, T. Sakamoto, K. Sasagawa, T. Kawanishi, M. Tsuchiya, G. R. A. Priem, D. Van Thourhout, P. Dumon, R. Baets, and H. K. Tsang, "Ultrafast all-optical switching by cross-absorption modulation in silicon wire waveguides," Opt. Express **13**, 7298–7303 (2005).

[13]P. Mehta, N. Healy, T. D. Day, J. R. Sparks, P. J. A. Sazio, J. V. Badding, and A. C. Peacock, "All-optical modulation using two-photon absorption in silicon core optical fibers," Opt. Express **19**, 19078–19083 (2011).

[14]V. R. Almeida, C. A. Barrios, R. R. Panepucci, and M. Lipson, "All-optical control of light on a silicon chip," Nature **431**, 1081–1084 (2004).

[15]A. C. Turner-Foster, M. A. Foster, J. S. Levy, C. B. Poitras, R. Salem, A. L. Gaeta, and M. Lipson, "Ultrashort free-carrier lifetime in low-loss silicon nanowaveguides," Opt. Express **18**, 3582–3591 (2010).

[16]M. Liu, X. Yin, and X. Zhang, "Double-layer graphene optical modulator," Nano Lett. **12**, 1482–1485 (2012).

[17]C. T. Phare, Y. D. Lee, J. Cardenas, and M. Lipson, "Graphene electro-optic modulator with 30 GHz bandwidth," Nat. Photonics **9**, 511–514 (2015).

[18]H. Dalir, Y. Xia, Y. Wang, and X. Zhang, "Athermal broadband graphene optical modulator with 35 GHz speed," ACS Photonics **3**, 1564–1568 (2016).

[19]V. Sorianello, M. Midrio, G. Contestabile, I. Asselberghs, J. Van Campenhout, C. Huyghebaert, I. Goykhman, A. K. Ott, A. C. Ferrari, and M. Romagnoli, "Graphene–silicon phase modulators with gigahertz bandwidth," Nat. Photonics **12**, 40–44 (2018).

[20]M. A. Giambra, V. Sorianello, V. Miseikis, S. Marconi, A. Montanaro, P. Galli, S. Pezzini, C. Coletti, and M. Romagnoli, "High-speed double layer graphene electroabsorption modulator on SOI waveguide," Opt. Express **27**, 20145–20155 (2019).

[21]D. Ansell, I. P. Radko, Z. Han, F. J. Rodriguez, S. I. Bozhevolnyi, and A. N. Grigorenko, "Hybrid graphene plasmonic waveguide modulators," Nat. Commun. **6**, 8846 (2015).

[22]S. Yan, X. Zhu, L. H. Frandsen, S. Xiao, N. A. Mortensen, J. Dong, and Y. Ding, "Slow-light-enhanced energy efficiency for graphene microheaters on silicon photonic crystal waveguides," Nat. Commun. **8**, 14411 (2017).

[23]L. Ye, K. Sui, Y. Zhang, and Q. H. Liu, "Broadband optical waveguide modulators based on strongly coupled hybrid graphene and metal nano-ribbons for near-infrared applications," Nanoscale **11**, 3229 (2019).

[24]Z. Cheng, X. Zhu, M. Galili, L. H. Frandsen, H. Hu, S. Xiao, J. Dong, Y. Ding, L. K. Oxenløwe, and X. Zhang, "Double-layer graphene on photonic crystal waveguide electro-absorption modulator with 12 GHz bandwidth," Nanophotonics (published online, 2019).

[25]W. Li, B. Chen, C. Meng, W. Fang, Y. Xiao, X. Li, Z. Hu, Y. Xu, L. Tong, H. Wang, W. Liu, J. Bao, and Y. R. Shen, "Ultrafast all-optical graphene modulator," Nano Lett. **14**, 955–959 (2014).

[26]Z. Cheng, H. K. Tsang, X. Wang, K. Xu, and J. Xu, "In-plane optical absorption and free-carrier absorption in graphene-on-silicon waveguides," IEEE J. Sel. Top. Quantum Electron. **20**, 4400106 (2014).

[27]J.-H. Chen, B.-C. Zheng, G.-H. Shao, S.-J. Ge, F. Xu, and Y.-Q. Lu, "An all-optical modulator based on a stereo graphene–microfiber structure," Light Sci. Appl. **4**, e360 (2015).

[28]Y. Wang, X. Gan, C. Zhao, L. Fang, D. Mao, Y. Xu, F. Zhang, T. Xi, L. Ren, and J. Zhao, "All-optical control of microfiber resonator by graphene's photothermal effect," Appl. Phys. Lett. **108**, 171905 (2016).

[29]S. Yu, X. Wu, K. Chen, B. Chen, X. Guo, D. Dai, L. Tong, W. Liu, and Y. R. Shen, "All-optical graphene modulator based on optical Kerr phase shift," Optica **3**, 541–544 (2016).

[30]M. Ono, M. Hata, M. Tsunekawa, K. Nozaki, H. Sumikura, H. Chiba, and M. Notomi, "Ultrafast and energy-efficient all-optical switching with graphene-loaded deep-subwavelength plasmonic waveguides," Nat. Photonics **14**, 37–43 (2020).

[31]H. Chen, C. Wang, H. Ouyang, Y. Song, and T. Jiang, "All-optical modulation with 2D layered materials: Status and prospects," Nanophotonics (published online, 2020).

[32]D. Brida, A. Tomadin, C. Manzoni, Y. J. Kim, A. Lombardo, S. Milana, R. R. Nair, K. S. Novoselov, A. C. Ferrari, G. Cerullo, and M. Polini, "Ultrafast collinear scattering and carrier multiplication in graphene," Nat. Commun. **4**, 1987 (2013).

[33]S. Sundaram and E. Mazur, "Inducing and probing non-thermal transitions in semiconductors using femtosecond laser pulses," Nat. Mater. **1**, 217–224 (2002).

[34]T. Li, D. Mao, N. W. Petrone, R. Grassi, H. Hu, Y. Ding, Z. Huang, G. Lo, J. C. Hone, T. Low, C. W. Wong, and T. Gu, "Spatially controlled electrostatic doping in graphene p-i-n junction for hybrid silicon photodiode," npj 2D Mater. Appl. **2**, 36 (2018).

[35]H. Zhou, T. Gu, J. F. McMillan, N. Petrone, A. Zande, J. C. Hone, M. Yu, G. Lo, D. Kwong, G. Feng, S. Zhou, and C. W. Wong, "Enhanced photoresponsivity in graphene-silicon slow-light photonic crystal waveguides," Appl. Phys. Lett. **108**, 111106 (2016).

[36]L. Song, X. Yu, and D. Yang, "A review on graphene-silicon Schottky junction interface," J. Alloys Compd. **806**, 63–70 (2019).

[37]N. Petrone, C. R. Dean, I. Meric, A. M. Zande, P. Y. Huang, L. Wang, D. Muller, K. L. Shepard, and J. Hone, "Chemical vapor deposition-derived graphene with electrical performance of exfoliated graphene," Nano Lett. **12**, 2751–2756 (2012).

[38]T. Gu, A. Andryieuski, Y. Hao, Y. Li, J. Hone, C. W. Wong, A. Lavrinenko, T. Low, and T. F. Heinz, "Photonic and plasmonic guided modes in graphene–silicon photonic crystals," ACS Photonics **2**, 1552–1558 (2015).

[39]A. Das, S. Pisana, B. Chakraborty, S. Piscanec, S. K. Saha, U. V. Waghmare, K. S. Novoselov, H. R. Krishnamurthy, A. K. Geim, A. C. Ferrari, and A. K. Sood, "Monitoring dopants by Raman scattering in an electrochemically top-gated graphene transistor," Nat. Nanotechnol. **3**, 210–215 (2008).

[40]M. Bruna, A. K. Ott, M. Ijäs, D. Yoon, U. Sassi, and A. C. Ferrari, "Doping dependence of the Raman spectrum of defected graphene," ACS Nano **8**(7), 7432–7441 (2014).